



OPEN Upconversion luminescence and temperature sensing characteristics of MgAl_2O_4 spinel doped with Er^{3+} and Yb^{3+} ions

Yang Lu¹, Jing Wang^{2✉}, Gang Wang^{1✉}, Zhongxiang Shi², Yu Jin¹ & Chaoran Deng¹

Nanorod-shaped $\text{MgAl}_2\text{O}_4: x\text{Er}^{3+}, 0.05\text{Yb}^{3+}$ (where x ranges from 0.003 to 0.015) were synthesized using a low-temperature hydrothermal method. This study investigates the microstructure, upconversion luminescence performance, and temperature sensing characteristics of these phosphors. Results indicate that with increasing Er^{3+} doping, lattice distortions due to vacancy defects and lattice expansion first increase and then decrease, peaking at an Er^{3+} doping concentration of 0.015. A calcination temperature of 1100 °C was determined to be economically optimal, with a total weight loss of 38.5% during the precursor calcination process. Under 980 nm excitation, the intensity and ratio of red to green emissions peaked at an Er^{3+} doping concentration of 0.01. By controlling the doping level of Er^{3+} and the pump current of the excitation light, the chromatic transition from yellow to green and color purity can be finely tuned. The maximum temperature sensitivity ($S_{a_{\text{max}}}$) based on thermally coupled levels for Er^{3+} in MgAl_2O_4 is $40.28 \times 10^{-4} \text{ K}^{-1}$, and based on non-thermally coupled levels, $S_{a_{\text{max}}}$ is $143.65 \times 10^{-4} \text{ K}^{-1}$, showing better performance than some common upconversion materials. Moreover, the calculated thermal activation energies for green and red transitions are $\Delta E_{545} = 0.4863 \text{ eV}$ and $\Delta E_{658} = 0.4203 \text{ eV}$, respectively. The high temperature sensitivity and thermal activation energies suggest that these phosphors are promising candidates for non-contact temperature sensing applications.

Keywords Mg-Al spinel, Upconversion luminescence, Temperature sensing characteristics

Luminescent materials have attracted significant attention due to their potential applications in optical devices and biomedical fields. To date, numerous studies and applications have been developed for various luminescent materials, including fluorescent proteins, organic dyes, metal complexes, noble metal nanoparticles, and rare-earth ion-doped inorganic luminophores. Among these, rare-earth ions, with their unique f-electron configurations that provide rich energy levels, exhibit distinctive optical properties in these doped upconversion luminescent materials. These properties include large anti-Stokes shifts (> 600 nm), strong peak emissions, long lifetimes, and excellent photothermal stability.

The application of rare-earth ion-doped upconversion luminescent materials in biomedicine demonstrates their ability to optimally absorb lower-energy and near-infrared photons (650–1100 nm), facilitating the emission process from ultraviolet to visible to near-infrared light. Due to the strong fluorescent radiation, long excited-state lifetimes, and rich radiative transition levels of Er^{3+} ions, the absorbed photons are readily distributed in the near-infrared region. Rare-earth Yb^{3+} ions are commonly used as sensitizing co-dopants in upconversion luminescent materials. Extensive research has been conducted on $\text{Er}^{3+}/\text{Yb}^{3+}$ co-doped upconversion phosphors. However, studies on upconversion luminescence processes in $\text{Er}^{3+}/\text{Yb}^{3+}$ co-doped MgAl_2O_4 are still limited¹. Choudhary et al.² employed a high-temperature solid-state method to obtain well-structured $\text{Er}^{3+}/\text{Yb}^{3+}$ co-doped MgAl_2O_4 , particularly using the addition of Bi^{3+} to significantly enhance the fluorescence intensity (mainly green light intensity), with a low intensity ratio of red to green light ($I_{\text{R}}/I_{\text{G}}$). Based on current application research, near-infrared or red light emission is more suitable for deep tissue imaging^{3,4}. Therefore, in the preliminary work of our research group, the effect of sensitizer Yb^{3+} on MgAl_2O_4 -based upconversion luminescence has been discussed, and the phosphor composition with high $I_{\text{R}}/I_{\text{G}}$ has been preliminarily obtained⁵. Especially,

¹Liaoning Provincial Engineering Research Center for High Value Utilization of Magnesite, Yingkou Institute of Technology, Yingkou 115014, China. ²Liaoning Key Laboratory for Fabrication and Application of Superfine Inorganic Powders, Dalian Jiaotong University, Dalian 116028, China. ✉email: wangjing@djtu.edu.cn; 33171733@qq.com

the unique chemical stability and high-temperature resistance of MgAl_2O_4 make it advantageous for complex applications such as deep tissue imaging and optical temperature sensing.

In this study, $\text{Er}^{3+}/\text{Yb}^{3+}$ co-doped MgAl_2O_4 phosphors were synthesized using a low-temperature hydrothermal method. The microstructure of the phosphor series was examined. Under 980 nm near-infrared light excitation, the upconversion luminescence performance of the phosphors was modulated by varying the activator Er^{3+} concentration and pump current. Using the fluorescence intensity ratio method (FIR), we analyzed the temperature sensing characteristics of Er^{3+} in the MgAl_2O_4 host material based on conventional thermally coupled and non-thermally coupled energy levels, and calculated its thermal activation energy, exploring its potential in non-contact optical temperature sensing applications.

Experiment

Sample Preparation

The raw materials $\text{Mg}(\text{NO}_3)_2 \cdot 6\text{H}_2\text{O}$ and $\text{Al}(\text{NO}_3)_3 \cdot 9\text{H}_2\text{O}$, both of analytical grade (purchased from Tianjin Damao Reagent in China), were accurately weighed according to the molar ratio of $n_{\text{Mg}^{2+}} : n_{\text{Al}^{3+}} = 1:2$. A specified amount of deionized water was added, and the mixture was stirred uniformly using a magnetic stirrer. The dopants $\text{Er}(\text{NO}_3)_3 \cdot 6\text{H}_2\text{O}$ and $\text{Yb}(\text{NO}_3)_3 \cdot 5\text{H}_2\text{O}$, both with a purity of 99.99% (purchased from Annegi Chemical Reagents), were prepared as rare-earth nitrate solutions at the required concentrations. These rare-earth nitrate solutions were then gradually added in accordance with the molar ratios of $\text{MgAl}_2\text{O}_4 : x\text{Er}^{3+}, 0.05\text{Yb}^{3+}$ (where x equals 0.003, 0.005, 0.007, 0.010, 0.012, 0.015), to the mixture of magnesium nitrate and aluminum nitrate, stirring continuously until a clear, homogeneous solution was obtained. The precipitating agent, urea, also of analytical grade (purchased from Tianjin Damao Reagent), was measured according to the molar ratio of $n_{\text{Mg}^{2+}} : n_{\text{Al}^{3+}} : n_{\text{Urea}} = 1:2:30$ and added to the nitrate solution. The mixture was stirred continuously for 30 min until completely dissolved. It is important to adjust the pH and volume of each sample of the mixed solution with deionized water, dilute nitric acid, and dilute ammonia to maintain approximate consistency, targeting a pH value of 3 and achieving an optimal volume at 80% of the reaction vessel's capacity. At this point, the total concentration of Mg^{2+} and Al^{3+} cations was 0.24 mol/L. The mixture was then poured into a 75 ml Teflon-lined stainless steel autoclave and heated at 120 °C for 24 h. The hydrothermal product was centrifuged at high speed (8000 rpm), washed alternately with deionized water and anhydrous ethanol several times, and dried in an 80 °C constant-temperature drying oven for 6 h. Finally, the dried precursor powder was calcined in a high-temperature furnace at 1100 °C for 3 h to obtain the $\text{MgAl}_2\text{O}_4 : \text{Er}^{3+}, \text{Yb}^{3+}$ series of phosphor powders.

Sample characterization

The crystal structure of the samples was characterized using a Malvern Panalytical X-ray diffractometer (operating at 50 mA and 35 kV, scanning range $2\theta = 10^\circ$ to 80°) with Cu-target $K\alpha$ radiation, $\lambda = 0.15406$ nm. The microstructure of the samples was observed using a Carl Zeiss SUPRA 55 field emission scanning electron microscope (SEM) at 5.0 kV. Phase transition analysis was performed using a STA449 synchronous thermal analyzer with a heating rate of 12 °C/min and a temperature range from room temperature to 1200 °C. Luminescent properties of the phosphor powders were analyzed using a Hitachi F-4600 fluorescence spectrometer, scanning from 400 to 750 nm at a rate of 1200 nm/min, excited by an ADR-1860 type 980 nm laser with a maximum operating current of 5.0 A. Temperature sensing measurements utilized a custom external temperature control system with a heating rate of 10 K/min and a temperature range from 273 to 600 K. The system was calibrated prior to testing.

Results and discussion

Microstructure of $\text{MgAl}_2\text{O}_4 : \text{Er}^{3+}, \text{Yb}^{3+}$ phosphor

The XRD results for the series of samples $\text{MgAl}_2\text{O}_4 : x\text{Er}^{3+}, 0.05\text{Yb}^{3+}$ (where $x = 0.003\text{--}0.015$) are shown in Fig. 1. The main diffraction peaks in the figure match those of MgAl_2O_4 (PDF NO.21-1152). Notably, the sample with 0.015 Er^{3+} doping shows a minor Er_2O_3 impurity peak at $2\theta = 26.2^\circ$ (Fig. 1(a)), while other samples do not exhibit obvious features of MgO , Al_2O_3 , or rare-earth oxide (Re_2O_3) impurities. This indicates that the rare earth ions $\text{Er}^{3+}/\text{Yb}^{3+}$ have entered the MgAl_2O_4 lattice and formed a uniform solid solution. Figure 1(b) presents a close-up view of the diffraction peak at the (311) plane for each sample. At 0.003 Er^{3+} doping, the peak shifts slightly to the right compared to the standard spinel. This shift is due to each Er^{3+} or Yb^{3+} ion non-equivalently occupying Mg^{2+} sites, creating a positive charge defect $[\text{Re}^{3+}]_{\text{Mg}}$. To maintain charge balance, a compensatory mechanism might form some cation vacancies (V'_{Mg}), causing lattice contraction and a shift of the diffraction peak to higher angles⁶. As Er^{3+} concentration increases, the larger ionic radius of Er^{3+} induces lattice expansion, gradually shifting peaks to lower angles until saturation at the 0.015 Er^{3+} doping. Table 1 summarizes calculated the unit cell parameters and crystallite sizes, demonstrating that the changes in cell parameters are consistent with the shifts in diffraction peaks, as shown in Fig. 1(c). Crystallite sizes initially decrease and then slightly increase with Er^{3+} doping, correlating with crystallinity changes induced by rare-earth incorporation.

Figure 2(a) displays the SEM image of undoped MgAl_2O_4 , primarily composed of 200 nm-diameter nanorods with smooth surfaces. After co-doping with 0.01 Er^{3+} and 0.05 Yb^{3+} , the nanorod structure persists but exhibits reduced uniformity and roughened surfaces (Fig. 2(b)). In conjunction with XRD analysis results (Fig. 1), the decrease in crystallinity with increasing Er^{3+} doping concentration can be attributed to damage to the crystal quality during the growth phase of MgAl_2O_4 crystals. The more rare earth ions that enter the main lattice, the easier it is to cause lattice distortions, leading to deterioration in crystallinity and surface morphology. The EDS elemental distribution map of the product shows a uniform distribution of Mg, Al, O, Er, and Yb elements throughout the product, with no localized elemental aggregation, indicating the uniform composition of the prepared spinel phosphor (Fig. 2(c)). EDS surface scanning of the co-doped samples provides the mass

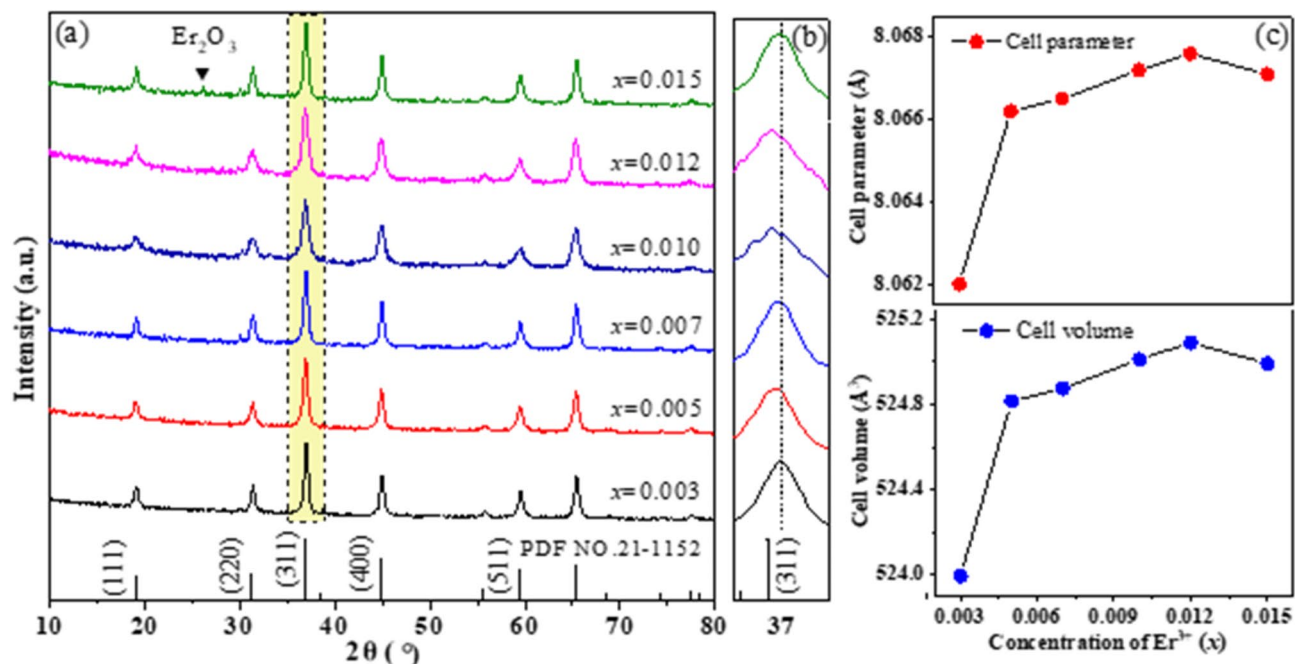


Fig. 1. (a) XRD patterns of the $\text{MgAl}_2\text{O}_4: x\text{Er}^{3+}, 0.05\text{Yb}^{3+}$ ($x = 0.003\text{--}0.015$) samples; (b) close-up view of the diffraction peak at the (311) plane for each sample; (c) the cell parameters and volumes of samples vary with doping concentration.

x	Cell parameter (Å)	Cell volume (Å ³)	Crystallite size (nm)
0.003	8.0620	523.9965	20.1
0.005	8.0662	524.8159	16.4
0.007	8.0665	524.8744	18.2
0.010	8.0672	525.0111	9.3
0.012	8.0676	525.0892	11.4
0.015	8.0671	524.9916	19.1

Table 1. Cell parameters and crystallite sizes of the $\text{MgAl}_2\text{O}_4: x\text{Er}^{3+}, 0.05\text{Yb}^{3+}$ samples.

percentages of each element (Fig. 3), revealing no other impurity elements. The main matrix elements, Mg, Al, and O, follow the typical spinel ratio closely, and trace elements Er and Yb are detectable at mass ratios of 4.8 wt% and 0.82 wt%, respectively, closely matching the doping content, indicating effective doping in the samples.

The $\text{MgAl}_2\text{O}_4: \text{Er}^{3+}, \text{Yb}^{3+}$ phosphor is a functional powder obtained by calcining the hydrothermal precursors. Therefore, the calcination temperature is crucial for the formation of the MgAl_2O_4 structure, necessitating the use of thermogravimetric-differential scanning calorimetry to further analyze the formation process of the MgAl_2O_4 structure. Figure 4 presents the TG-DSC analysis of the precursor of the $\text{MgAl}_2\text{O}_4: 0.01\text{Er}^{3+}, 0.05\text{Yb}^{3+}$ sample. Total weight loss from 20 °C to 1200 °C is 38.5 wt%, primarily occurring between 20 °C and 500 °C, with four distinct stages, each correlating with endothermic peaks on the DSC curve. The first stage of TG weight loss occurs between 50 °C and 150 °C, attributed to the removal of large amounts of free water and the evaporation of residual organic alcohols from washing. The second stage, between 170 °C and 220 °C, involves the decomposition of the ammonium aluminum carbonate precursor to form active aluminum oxide. The third stage centers around a sharp endothermic peak at 275 °C, where significant weight loss occurs due to the precursor of magnesium aluminum hydroxalate shedding a substantial amount of hydroxyl groups, thereby forming a uniform magnesium aluminum solid solution. The fourth stage corresponds to a broad endothermic peak between 350 °C and 800 °C, peaking around 500 °C. Studies suggest that at 500 °C, the layered structure of magnesium aluminum hydroxalate transforms into an amorphous magnesium aluminum solid solution, and as the temperature increases, MgAl_2O_4 is directly formed along with the generation of an MgO phase⁷. No significant weight loss above 800 °C indicates non-reconstructive phase transitions, involving rearrangement of Mg^{2+} and Al^{3+} sublattices without oxygen lattice changes, requiring less energy. Notably, at 1100 °C, the DSC curve shows a clear absorption peak without weight loss, indicating a significant spinel phase transformation due to the decomposition of the magnesium aluminum hydroxalate and ammonium aluminum carbonate precursors and the subsequent diffusion and reaction of the active MgO and Al_2O_3 at the phase boundaries, extensively producing MgAl_2O_4 (Eqs. (1)–(3))⁸, validating the 1100 °C calcination temperature selection.

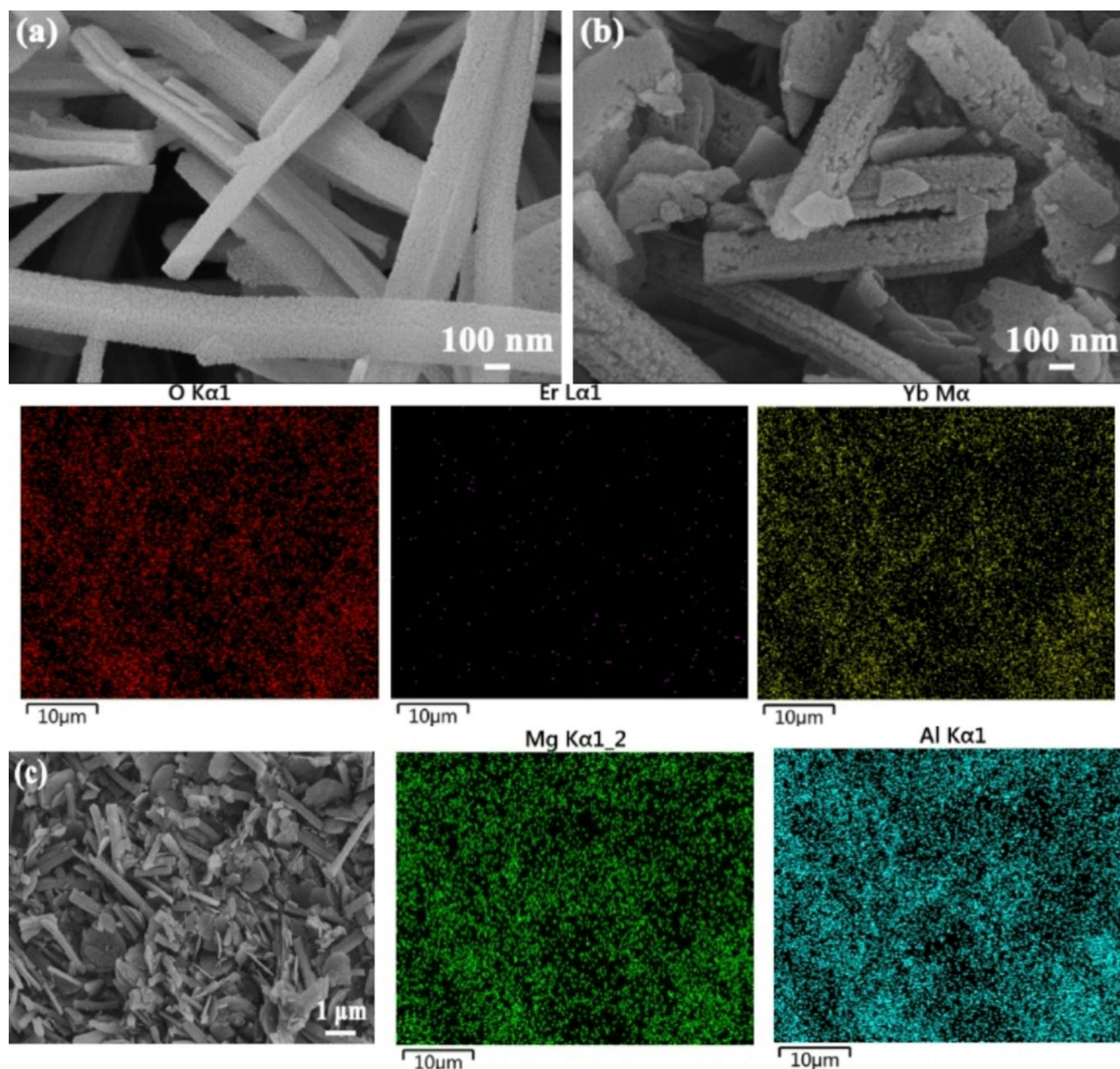
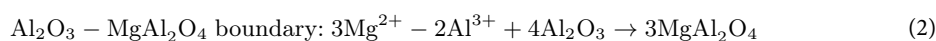
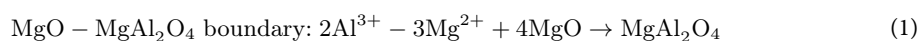


Fig. 2. (a) SEM image of undoped MgAl_2O_4 ; (b, c) SEM and EDS elemental distribution maps of the MgAl_2O_4 : 0.01Er^{3+} , 0.05Yb^{3+} .



Upconversion luminescence performance of MgAl_2O_4 : Er^{3+} , Yb^{3+} phosphor

Impact of the activator Er^{3+} ion

The upconversion luminescence performance of MgAl_2O_4 : $x\text{Er}^{3+}$, 0.05Yb^{3+} ($x=0.003$ – 0.015) phosphors under 980 nm light excitation is illustrated in Fig. 5. Figure 5(a) shows three primary emission peaks at 524 nm, 545 nm (green), and 658 nm (red), corresponding to the Er^{3+} transitions ${}^2\text{H}_{11/2} \rightarrow {}^4\text{I}_{15/2}$, ${}^4\text{S}_{3/2} \rightarrow {}^4\text{I}_{15/2}$, and ${}^4\text{F}_{9/2} \rightarrow {}^4\text{I}_{15/2}$, respectively. Both green and red emission intensities vary systematically with Er^{3+} concentration. Figure 5(b) presents the integrated intensity of the red and green emission bands and the ratio of red to green light intensity ($I_{\text{R}}/I_{\text{G}}$) as a function of Er^{3+} doping concentration. The red emission dominates, peaking at $x=0.01$ before declining due to concentration quenching (Fig. 5(b)). The $I_{\text{R}}/I_{\text{G}}$ ratio reaches a maximum of 6.4 at $x=0.01$. Consequently, as the Er^{3+} doping concentration increases from 0.003 to 0.01, the luminescent region of the phosphor linearly shifts from the green to the red region (Fig. 5(c)). Based on these changes in upconversion

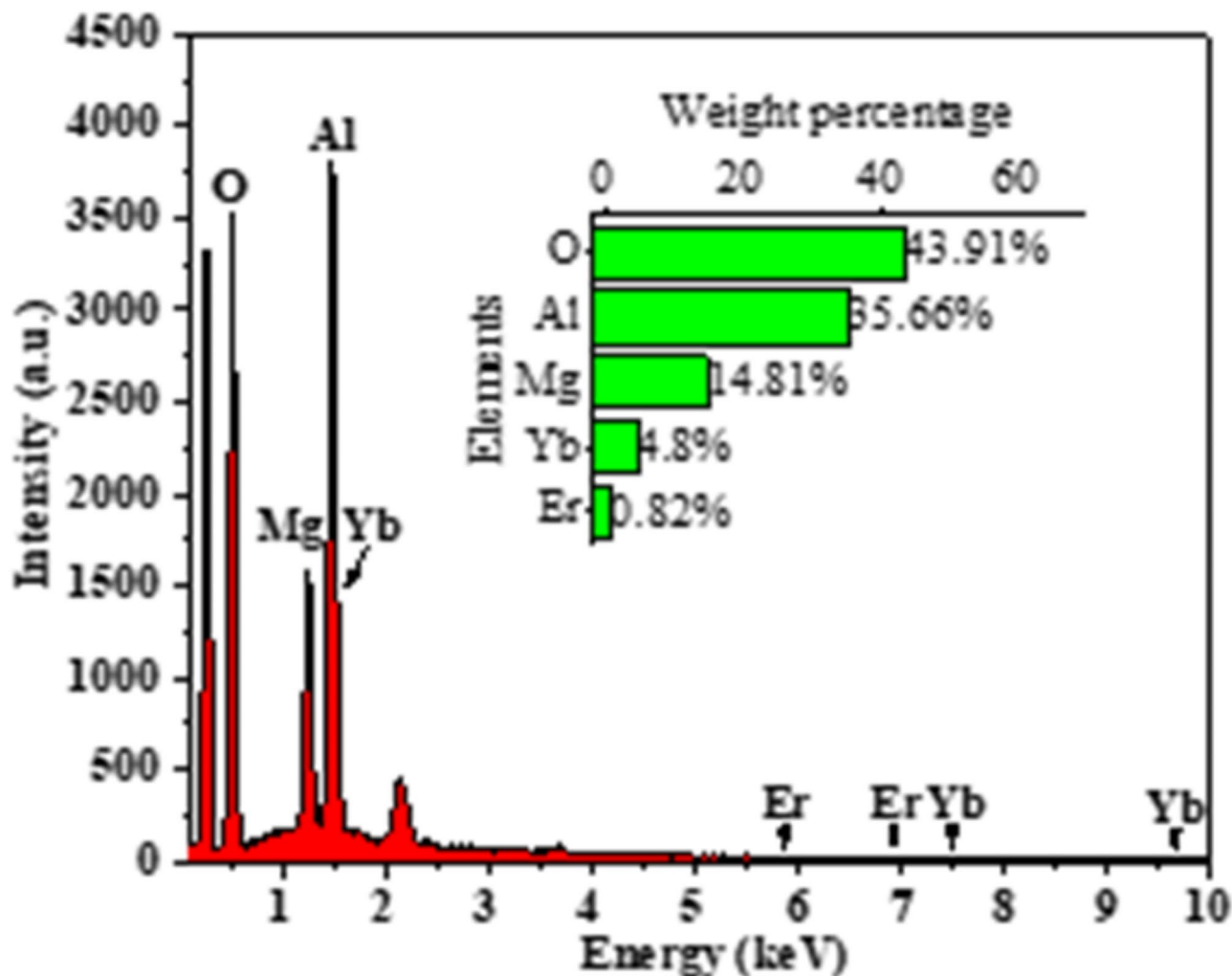


Fig. 3. EDS elemental content composition of $\text{MgAl}_2\text{O}_4:0.01\text{Er}^{3+}, 0.05\text{Yb}^{3+}$.

luminescence performance, a possible luminescence mechanism diagram is illustrated in Fig. 5(d). Analysis indicates that as the Er^{3+} doping concentration increases to 0.01, it promotes the energy transfer (ET1, ET2, and ET3) processes (Eqs. (4)–(6)), increasing the population of the $^2H_{11/2}$, $^4S_{3/2}$, and $^4F_{9/2}$ energy levels, thereby enhancing both red and green light intensities. Additionally, cross-relaxation (CR) processes (Eq. (7)) between Er^{3+} ions increase the population at the $^4I_{13/2}$ level, which is favorable for enhancing the population at the $^4F_{9/2}$ level through the ET3 process, thus intensifying the red light emission, making it significantly stronger than the green light. Furthermore, as the Er^{3+} doping concentration exceeds 0.01, the reduced distance between Er^{3+} ions facilitates energy transfer between Er^{3+} ions and the back energy transfer (EBT) process from Er^{3+} to Yb^{3+} (Eq. (8)), which are likely the primary causes of concentration quenching observed in this case.

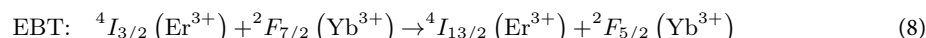
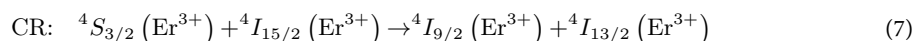
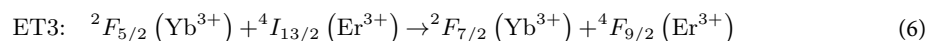
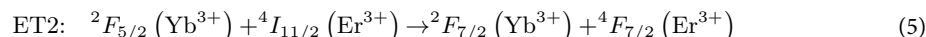
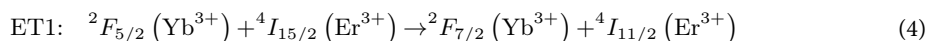


Table 2 provides details on the specific chromatic coordinates (X, Y), correlated color temperature (CCT), dominant wavelength (WLD), coloration, and color purity of the phosphor series. The results indicate that with increasing Er^{3+} doping concentration, the sample displays a multicolor transition from yellow-green to pure yellow and back to yellow-green. The $\text{MgAl}_2\text{O}_4:0.01\text{Er}^{3+}, 0.05\text{Yb}^{3+}$ sample exhibits the best color quality, with a color purity of 96.28%, a dominant wavelength of 577.46 nm, and a color temperature of 2913 K, representing a high-purity, warm-toned yellow light emission.

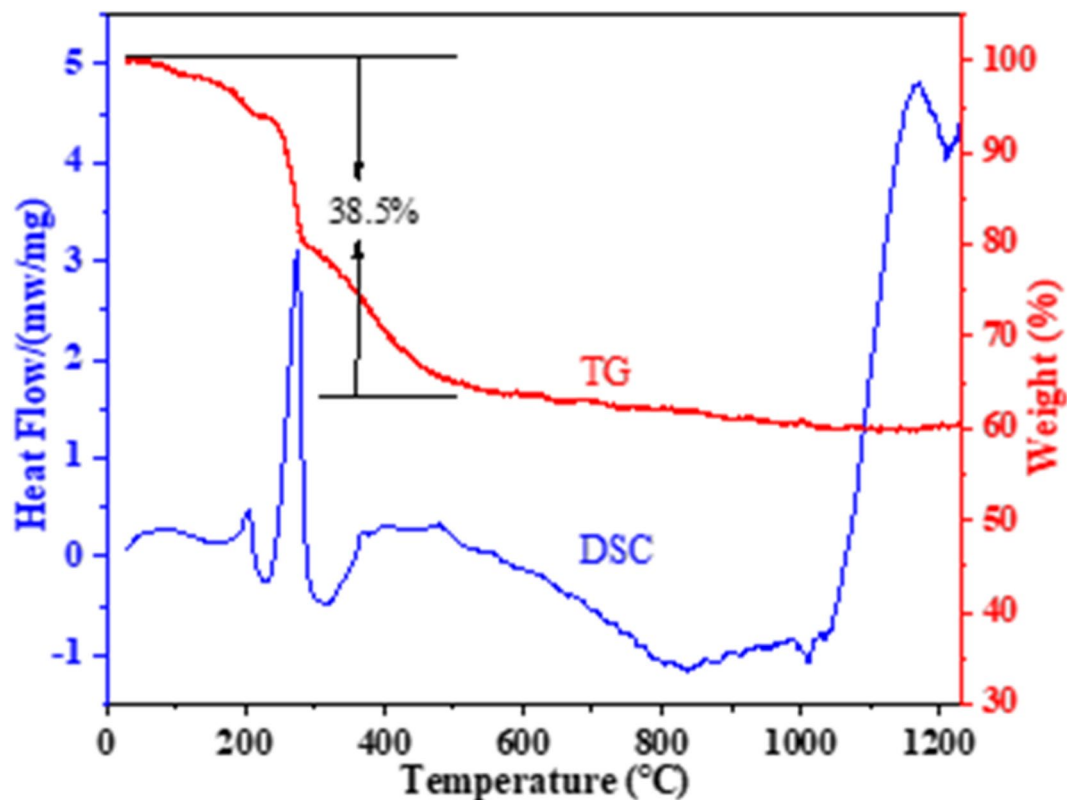


Fig. 4. TG-DSC analysis of the precursor for $\text{MgAl}_2\text{O}_4: 0.01\text{Er}^{3+}, 0.05\text{Yb}^{3+}$.

Impact of pump current

Under light excitation at $\lambda_{\text{ex}} = 980 \text{ nm}$, the upconversion luminescence performance of $\text{MgAl}_2\text{O}_4: 0.01\text{Er}^{3+}, 0.05\text{Yb}^{3+}$ sample was analyzed across various pump currents ranging from 0.8 to 2.0 A, as illustrated in Fig. 6. Figure 6(a) shows that the positions of the emission peaks remain unchanged with varying pump currents; however, the intensities of the red and green emissions increase progressively with higher currents. Figure 6(b) evaluates the integrated intensity of the red and green emission bands and the ratio of red to green light intensity ($I_{\text{R}}/I_{\text{G}}$) as a function of the pump current. It is evident that as the pump current increases, both the red and green light integrated intensities monotonically increase, while the $I_{\text{R}}/I_{\text{G}}$ ratio decreases from 8.29 to 2.85. This indicates a difference in the rate of intensity increase between the red and green light; the intensity of high-energy level upconversion luminescence (green light) increases faster than that of the low-energy level (red light). Consequently, the slower increase in red light intensity leads to changes in the $I_{\text{R}}/I_{\text{G}}$ ratio, ultimately affecting the optical output.

On the other hand, the magnitude of the pump current influences the population of Er^{3+} energy levels, which may be the underlying reason for the changes in the integrated intensity of the red and green emission bands and the $I_{\text{R}}/I_{\text{G}}$ ratio with pump current. As demonstrated in the upconversion luminescence mechanism chart (Fig. 5(d)), red light is produced at the lower energy level ${}^4F_{9/2}$ of Er^{3+} , while green light originates from the higher energy level ${}^4F_{7/2}$. At lower pump currents, electrons are more likely to transition to the lower energy level ${}^4F_{9/2}$, resulting in a larger $I_{\text{R}}/I_{\text{G}}$ ratio. However, with increasing pump current, the energy available to electrons rises, equalizing the probabilities of transitioning to both lower and higher energy levels. This leads to a gradual decrease in the $I_{\text{R}}/I_{\text{G}}$ ratio, and the output light shifts linearly from the red to the green region, as depicted in Fig. 6(c).

Table 3 presents the colorimetric data of the upconversion phosphor under varying pump currents. The results show that as the pump current increases, the color temperature of the phosphor rises from 2502 K to 4272 K, shifting the hue progressively cooler, with the dominant wavelength moving from 581.27 nm to 565.87 nm, and the color purity decreasing from 96.60 to 92.40%. The color transition moves from pure yellow to greenish yellow to yellow-green. Evidently, when disregarding luminescence intensity, appropriately reducing the pump current can effectively lower the phosphor's color temperature, enhance the red component and color purity, and achieve a purer warm-toned light emission. This provides a richer set of options for expanding the applications of $\text{MgAl}_2\text{O}_4: \text{Er}^{3+}, \text{Yb}^{3+}$ upconversion phosphor.

Temperature sensing characteristics

Temperature measurement based on the fluorescence intensity ratio (FIR) of rare earth ions typically differentiates between thermally coupled levels (TCLs) and non-thermally coupled levels (NTCLs). In TCLs, the energy difference between emitting levels should be close, falling within the range of 200 to 2000 cm^{-1} . In contrast,

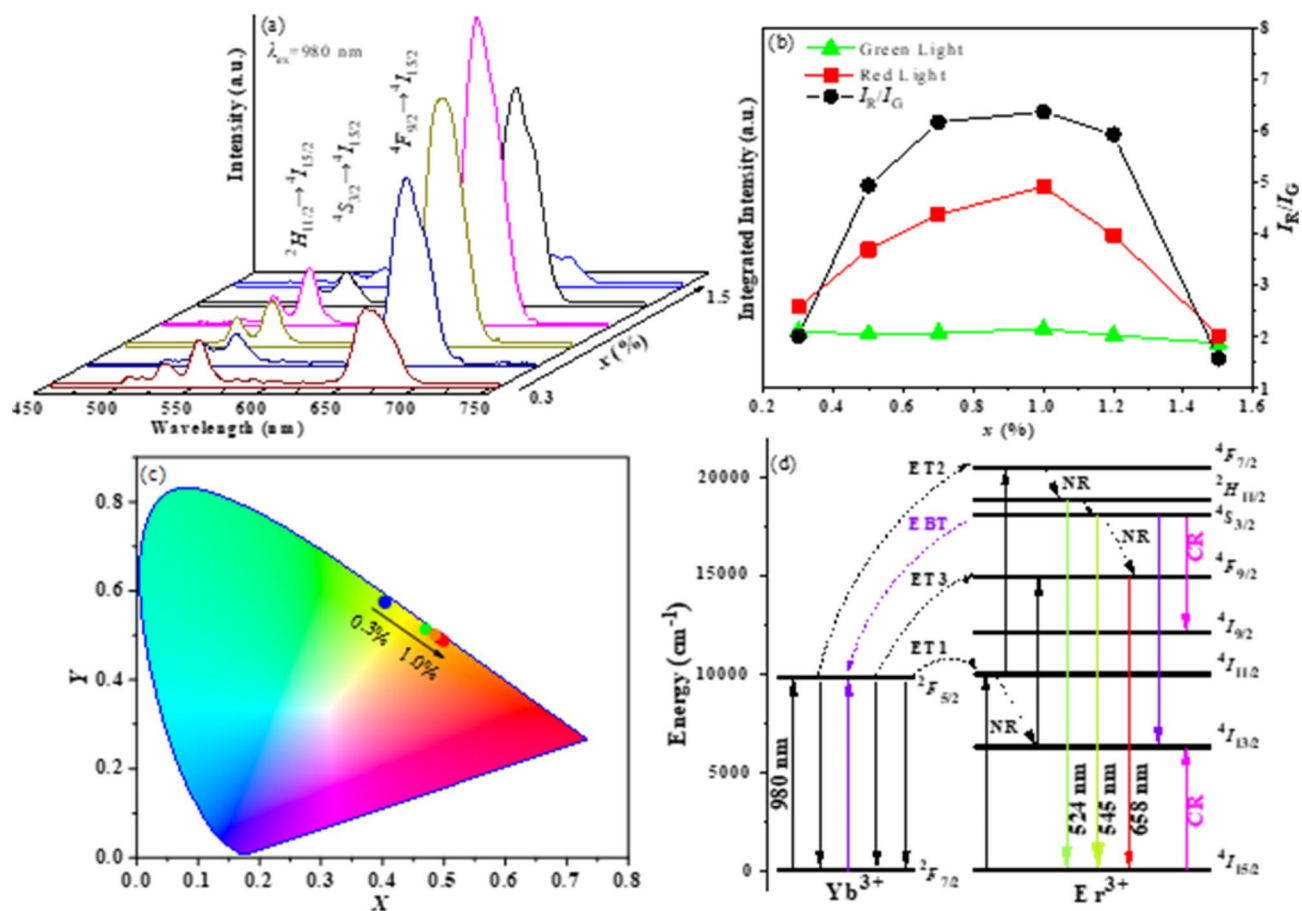


Fig. 5. (a) Upconversion emission spectra; (b) The relationship between the intensity and ratio of red and green light as a function of x ; (c) CIE chromaticity diagram; (d) Proposed luminescence mechanism diagram.

x	Chromatic coordinates	CCT (K)	WLD (nm)	Coloration	Color purity (%)
0.003	(0.4025, 0.5763)	4394	564.73	Yellow-green	94.10
0.005	(0.4702, 0.5139)	3234	574.68	Greenish yellow	95.53
0.007	(0.4880, 0.4987)	2938	577.23	Yellow	96.22
0.010	(0.4894, 0.4971)	2913	577.46	Yellow	96.28
0.012	(0.4852, 0.5011)	2983	576.83	Yellow	96.19
0.015	(0.4042, 0.5738)	4362	565.02	Yellow-green	93.86

Table 2. Chromatic coordinates (X , Y), correlated color temperature (CCT), dominant wavelength (WLD), coloration, and color purity of the samples with varying x .

an energy difference exceeding 2000 cm^{-1} defines NTCLs. A commonly used pair of TCLs for Er^{3+} involves the green light transitions ${}^2H_{11/2} \rightarrow {}^4I_{15/2}$ and ${}^4S_{3/2} \rightarrow {}^4I_{15/2}$, with an energy difference of approximately 700 cm^{-1} . Meanwhile, the energy gap between the levels ${}^4S_{3/2} \rightarrow {}^4I_{15/2}$ and ${}^4F_{9/2} \rightarrow {}^4I_{15/2}$ reaches 3000 cm^{-1} , constituting an NTCL between the red and green emissions. Previous studies have incorporated rare earth ions such as Er^{3+} and Yb^{3+} into various host materials to achieve high sensitivity in temperature sensing^{9–12}. However, discussions on FIR technology for temperature measurement using $\text{MgAl}_2\text{O}_4: \text{Er}^{3+}/\text{Yb}^{3+}$ phosphors remain sparse. Choudhary et al.² discussed the temperature sensing characteristics of the $\text{MgAl}_2\text{O}_4: \text{Er}^{3+}/\text{Yb}^{3+}$ phosphor series, noting that the introduction of Bi^{3+} as a dopant significantly enhanced the green emission intensity and improved the temperature sensing sensitivity based on the thermally coupled green light levels. Nonetheless, the $\text{MgAl}_2\text{O}_4: \text{Er}^{3+}/\text{Yb}^{3+}$ upconversion phosphors prepared in this work exhibited a higher red-to-green light intensity ratio, with the green light noticeably weaker than the red. This disparity could disadvantage discussions on the temperature sensitivity and potential applications of the thermally coupled green light levels ${}^2H_{11/2} \rightarrow {}^4I_{15/2}$ and ${}^4S_{3/2} \rightarrow {}^4I_{15/2}$. Furthermore, discussions on the FIR technology involving Er^{3+} 's red and green NTCLs in $\text{MgAl}_2\text{O}_4: \text{Er}^{3+}/\text{Yb}^{3+}$ phosphors are still scarce to date, necessitating a comparative analysis of the luminescence and temperature-dependent characteristics based on the thermally (green) and non-thermally (red-green) coupled levels in these

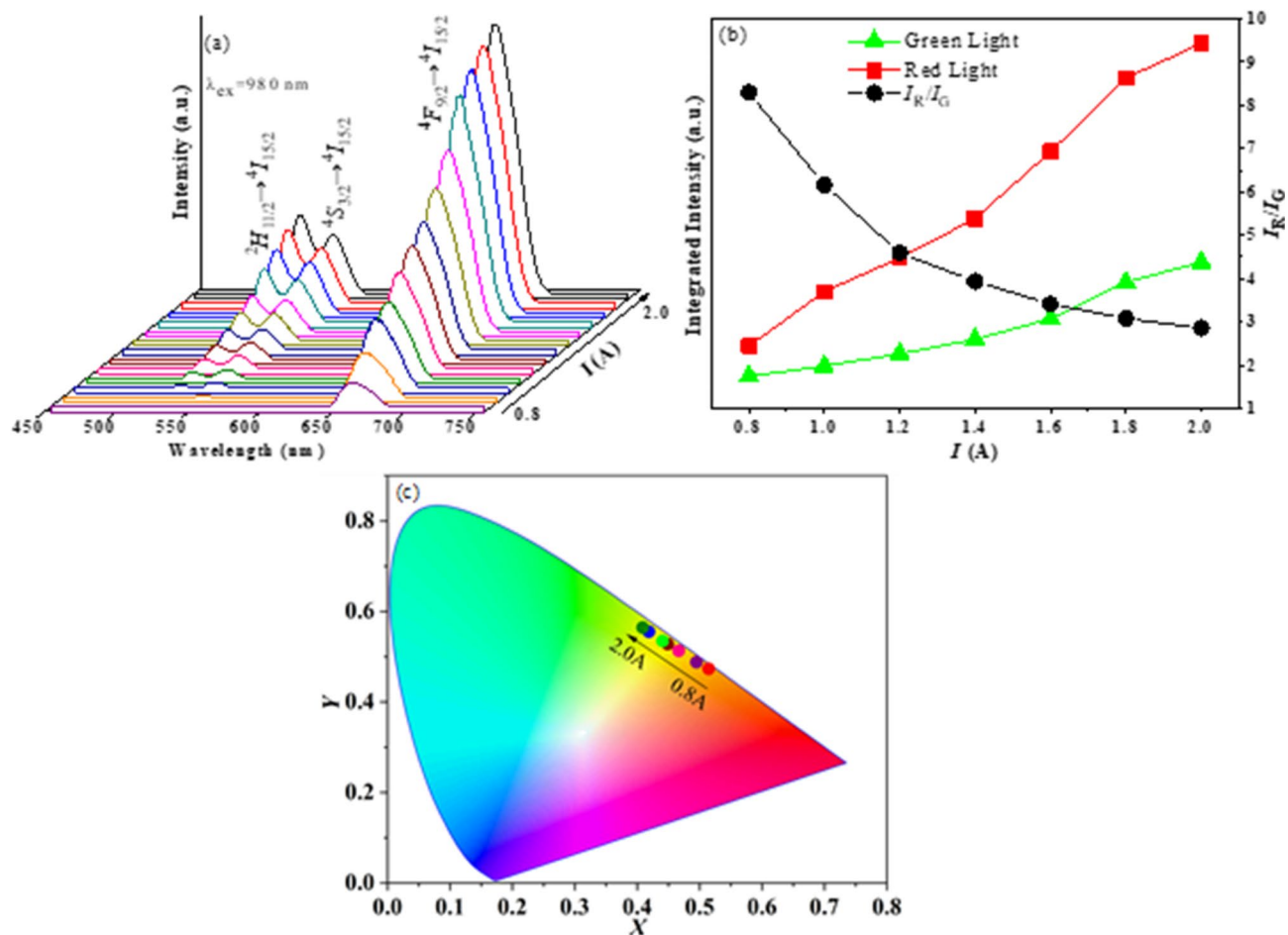


Fig. 6. (a) Emission spectra under different pump currents; (b) The relationship between the intensity and ratio of red and green light as a function of pump current; (c) CIE chromaticity diagram.

I (A)	Chromatic coordinates	CCT (K)	WLD (nm)	Coloration	Color purity (%)
0.8	(0.5145, 0.4733)	2502	581.27	Yellow	96.60
1.0	(0.4948, 0.4880)	2798	578.59	Yellow	95.11
1.2	(0.4663, 0.5133)	3278	574.39	Greenish yellow	94.18
1.4	(0.4487, 0.5282)	3143	571.83	Greenish yellow	93.39
1.6	(0.4407, 0.5349)	3717	570.67	Yellow-green	93.00
1.8	(0.4187, 0.5556)	4101	567.35	Yellow-green	92.66
2.0	(0.4087, 0.5645)	4272	565.87	Yellow-green	92.40

Table 3. Chromatic coordinates (X , Y), correlated color temperature (CCT), dominant wavelength (WLD), coloration, and color purity of the samples under varying pump currents.

upconversion phosphors. Due to the better optical properties exhibited by the low-quenching-concentration doping sample, the $\text{MgAl}_2\text{O}_4: 0.01\text{Er}^{3+}, 0.05\text{Yb}^{3+}$ sample was chosen for thermosensitive measurements in this study.

Temperature sensing properties of Er^{3+} based on TCLs

Under 980 nm excitation, we monitored the green light emission spectra formed by the transitions of TCLs (${}^2\text{H}_{11/2} \rightarrow {}^4\text{I}_{15/2}$ and ${}^4\text{S}_{3/2} \rightarrow {}^4\text{I}_{15/2}$) in the sample. As the heating temperature increased from 323 K to 583 K, these spectra exhibited systematic changes within the 500–600 nm range, as shown in Fig. 7(a). Figure 7(b) displays the relationship between the integrated emission peak intensities (I_{524} and I_{545}) of these levels and temperature. I_{545} predominantly shows a monotonic decrease with increasing temperature, while I_{524} initially weakens slightly and then begins to increase at 383 K, reaching a maximum at 443 K before gradually decreasing. This pattern is due to enhanced non-radiative transitions and cross-relaxation processes between the ${}^2\text{H}_{11/2} \rightarrow {}^4\text{I}_{15/2}$

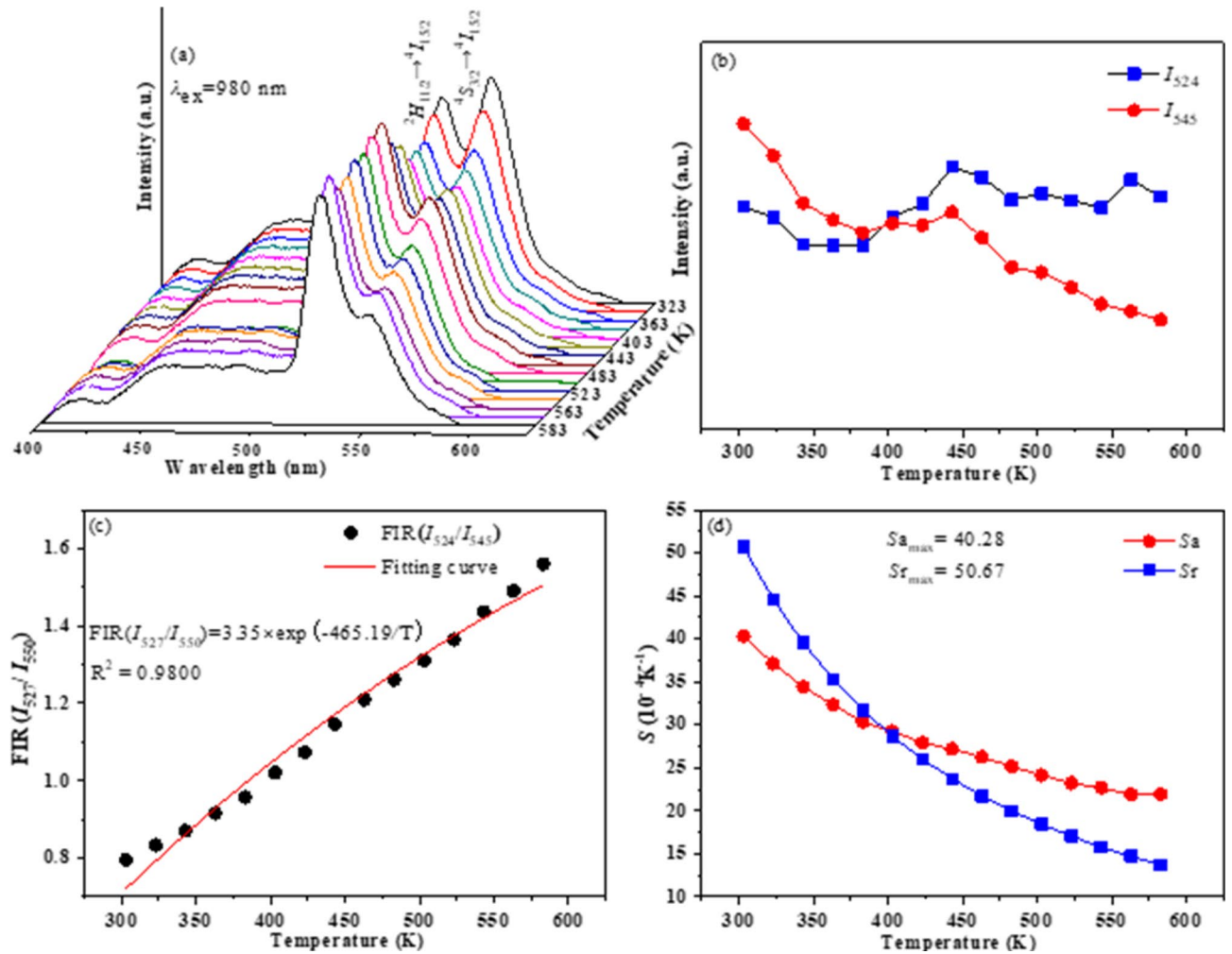


Fig. 7. (a) Temperature-dependent upconversion emission spectra of $\text{MgAl}_2\text{O}_4: 0.01\text{Er}^{3+}, 0.05\text{Yb}^{3+}$ at different temperatures; (b) The relationship between the integrated emission peak intensities (I_{524} and I_{545}) and temperatures; (c) The FIR ratio as a function of temperature; (d) Temperature dependence of sensitivities for the TCLs.

and $^4\text{S}_{3/2} \rightarrow ^4\text{I}_{15/2}$ levels as temperature increases, ultimately leading to a noticeable thermal quenching effect in the sample's thermally coupled green light levels. The temperature-dependent FIR technique, $\text{FIR} = I_{524}/I_{545}$, is plotted against temperature changes in Fig. 7(c), showing a definite temperature dependence. This dependence fits well with a Boltzmann distribution, as indicated by the formula (9):

$$\text{FIR} = \frac{I_{527}}{I_{550}} = C \exp\left(-\frac{\Delta E}{kT}\right) \quad (9)$$

$$S_a = \left| \frac{d\text{FIR}}{dT} \right| = \text{FIR} \frac{\Delta E}{kT^2} \quad (10)$$

$$S_r = \left| \frac{1}{\text{FIR}} \frac{d\text{FIR}}{dT} \right| = \frac{\Delta E}{kT^2} \quad (11)$$

Where C is a constant, ΔE is the energy gap between the two TCLs, k is the Boltzmann constant, and T is the absolute temperature. The fitted result is $\text{FIR} = 3.35 \times \exp(-465.19/T)$. Additionally, sensitivity as a critical parameter for assessing temperature sensing performance, includes both absolute sensitivity (S_a) and relative sensitivity (S_r), which are calculated using Eqs. (11)–(13).

The results shown in Fig. 7(d) indicate that both S_a and S_r values monotonically decrease as temperature increases. At a sample temperature of 323 K, the maximum sensitivity values obtained for temperature sensing based on TCLs are $S_{a_{\max}} = 40.28 \times 10^{-4} \text{ K}^{-1}$ and $S_{r_{\max}} = 50.67 \times 10^{-4} \text{ K}^{-1}$. It is evident that the temperature sensing sensitivity of Er^{3+} based on TCLs in the MgAl_2O_4 matrix does not show a significant advantage over other substrate materials. Due to the small energy gap between TCLs, and considering that larger energy gaps lead to higher temperature measurement sensitivity, the distance between these levels is disadvantageous for enhancing

optical temperature sensing sensitivity^{13,14}. Therefore, it is necessary to explore the temperature sensing sensitivity of Er³⁺ in the MgAl₂O₄ matrix based on NTCLs.

Temperature sensing properties of Er³⁺ based on NTCLs

Most rare earth ions exhibit NTCLs, offering a broader selection for FIR techniques based on NTCLs. As the sample's temperature increased from 323 K to 583 K, we monitored the red and green band emission spectra formed by the transitions from NTCLs ($^2H_{11/2} \rightarrow ^4I_{15/2}$ and $^4F_{9/2} \rightarrow ^4I_{15/2}$). These spectra displayed systematic shifts in the 500–700 nm range, as illustrated in Fig. 8(a). Figure 8(b) presents the relationship between the integrated emission peak intensities (I_{524} and I_{658}) of these transitions and temperature. As the temperature rose, I_{658} showed a more pronounced decrease, indicating a significant temperature quenching effect at the $^4F_{9/2} \rightarrow ^4I_{15/2}$ level due to non-radiative transitions and cross-relaxation processes. The temperature-dependent fluorescence intensity ratio (FIR = I_{524}/I_{658}) is plotted in Fig. 8(c), showing a clear temperature dependency. The larger gap between NTCLs, which cannot be easily filled through thermal excitation, allows for this temperature dependency to be well-fitted by a polynomial function, as shown in Fig. 8(d).

$$FIR = \frac{I_{527}}{I_{662}} = A + BT + CT^2 + DT^3 \quad (12)$$

The constants A, B, C, and D in the polynomial, where T is the absolute temperature, lead to the fit $FIR = 3.01 + 0.04T - 1.33E-04 \times T^2 + 1.16E-07 \times T^3$. Using Eqs. (14)–(15), we calculated the S_a and S_r based on NTCLs, as shown in Fig. 8(d).

$$S_a = \left| \frac{dFIR}{dT} \right| = B + 2CT + 3DT^2 \quad (13)$$

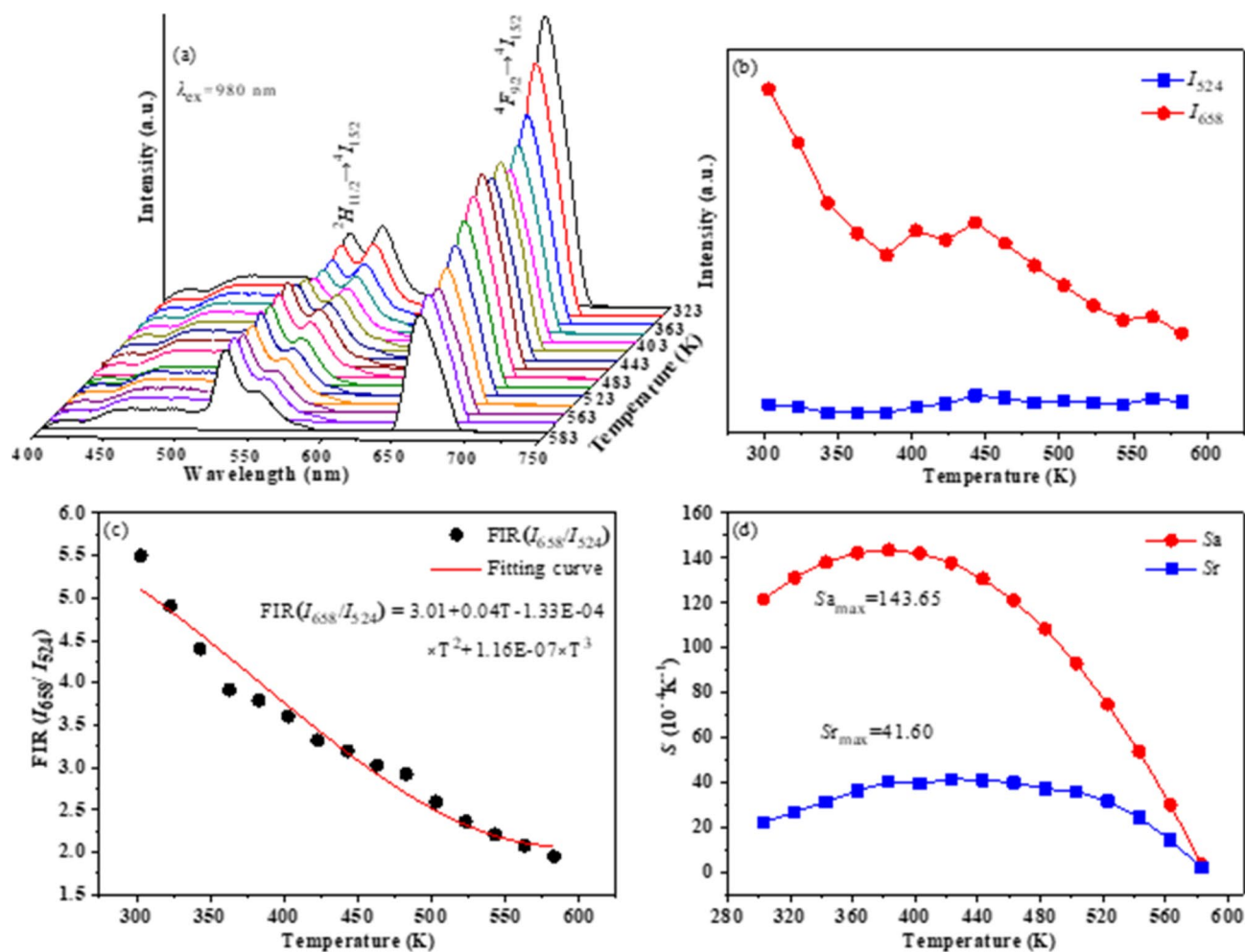


Fig. 8. (a) Temperature-dependent upconversion emission spectra of MgAl₂O₄:0.01Er³⁺, 0.05Yb³⁺ at different temperatures; (b) The relationship between the integrated emission peak intensities (I_{524} and I_{658}) and temperatures; (c) The FIR ratio as a function of temperature; (d) Temperature dependence of sensitivities for the NTCLs.

Upconversion phosphor	Transition energy level	T (K)	Sa _{max} (10 ⁻⁴ K ⁻¹)	References
NaGdF ₄ : Ho ³⁺ /Yb ³⁺	⁵ F ₄ , ⁵ F ₂ → ⁵ I ₈	303–523	51	15
Ba ₉ Y ₂ Si ₆ O ₂₄ : Yb ³⁺ /Ln ³⁺	⁵ F ₄ , ⁵ S ₂ → ⁵ F ₅	293–553	58	16
NaLaMgWO ₆ : Er ³⁺ /Yb ³⁺	⁵ F ₄ , ⁵ S ₂ → ⁵ F ₅	293–553	89	17
NaLuF ₄ : Yb ³⁺ /Er ³⁺ /Tm ³⁺	³ F ₂ → ³ H ₆ , ⁴ F _{9/2} → ⁴ I _{15/2}	300–600	76	18
NaYF ₄ : Yb ³⁺ /Tm ³⁺	¹ I ₆ → ³ F ₄ , ³ F _{2,3} → ³ H ₄	303–443	24	19
NaLa(WO ₄) ₂ : Er ³⁺ /Yb ³⁺	² H _{11/2} , ⁴ S _{3/2} → ⁴ I _{15/2}	300–510	131	20
MgAl ₂ O ₄ : Er ³⁺ /Yb ³⁺	² H _{11/2} , ⁴ F _{9/2} → ⁴ I _{15/2}	323–583	144	This work

Table 4. FIR parameters, maximum sensitivity (Sa_{max}), and optimal temperatures of Er³⁺/Yb³⁺-doped materials.

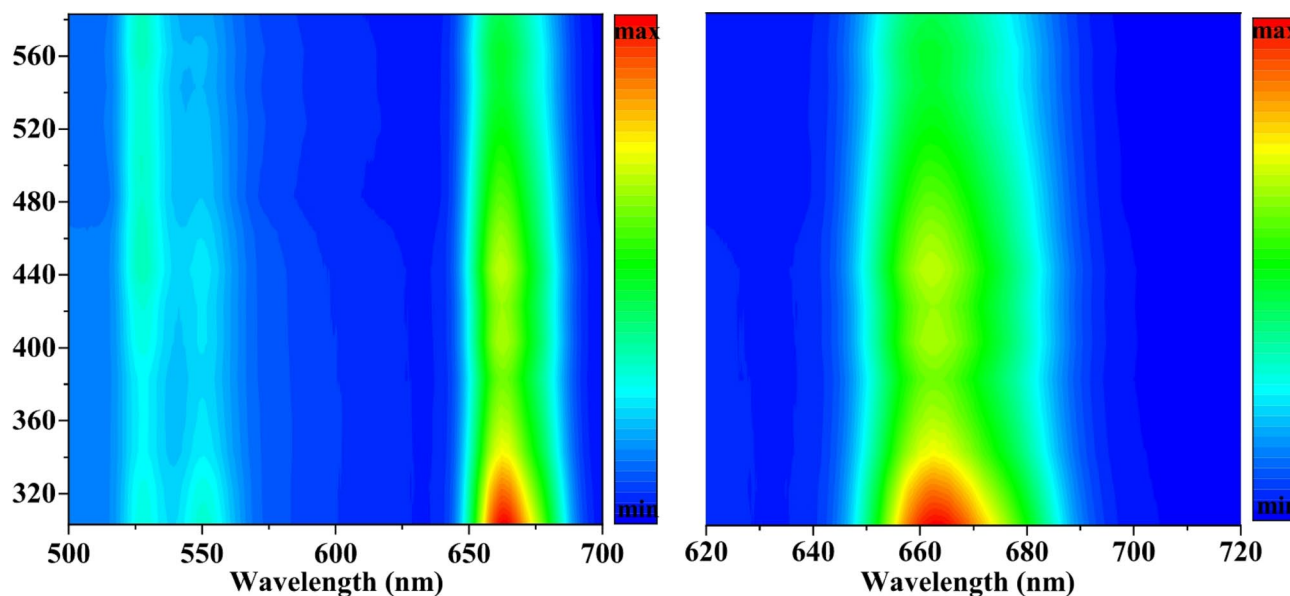


Fig. 9. Temperature-dependent emission spectra contour maps of MgAl₂O₄: Er³⁺, Yb³⁺ in the green and red regions.

$$S_r = \left| \frac{1}{\text{FIR}} \frac{d\text{FIR}}{dT} \right| = (B + 2CT + 3DT^2)/\text{FIR} \quad (14)$$

The results indicate that both Sa and Sr values initially increase and then decrease with rising temperatures, a behavior distinctly different from the monotonic decrease observed with TCLs. The maximum sensitivity values for temperature sensing based on NTCLs were achieved at temperatures of 383 K and 423 K, with Sa_{max} = 143.65 × 10⁻⁴ K⁻¹ and Sr_{max} = 41.60 × 10⁻⁴ K⁻¹, respectively. Additionally, we summarized the optical temperature sensing sensitivity of Er³⁺ and Yb³⁺ doped in other host materials, as shown in Table 4. Clearly, the sensitivity exhibited by MgAl₂O₄: Er³⁺, Yb³⁺ phosphors based on NTCLs surpasses that of some common upconversion materials, suggesting that MgAl₂O₄ is a promising host material for temperature sensing applications.

Photothermal stability

To vividly demonstrate the photothermal stability of the prepared MgAl₂O₄: Er³⁺, Yb³⁺ phosphors, temperature-dependent emission spectra contour maps were plotted within the green (500–600 nm) and red (620–720 nm) light regions, as shown in Fig. 9, covering a temperature range from 303 K to 583 K. The maps indicate that the emission bandwidths of the sample are minimally affected by temperature, suggesting notable color stability under high temperatures. Notably, the green light intensity near 524 nm does not decrease with increasing temperature, whereas the green and red light intensities near 545 nm and 658 nm exhibit significant thermal quenching effects.

It is generally accepted that the temperature at which the luminous intensity drops to 50% of its initial value is defined as the thermal quenching temperature, commonly denoted as T_{0.5}. Based on the normalized integrated green and red light intensities (I₅₄₅ and I₆₅₈) and their temperature dependencies as shown in Fig. 10, the thermal quenching temperatures for green and red emissions are determined to be 583 K and 503 K, respectively, suggesting superior thermal stability of the green emission. Utilizing the thermal quenching mechanism of

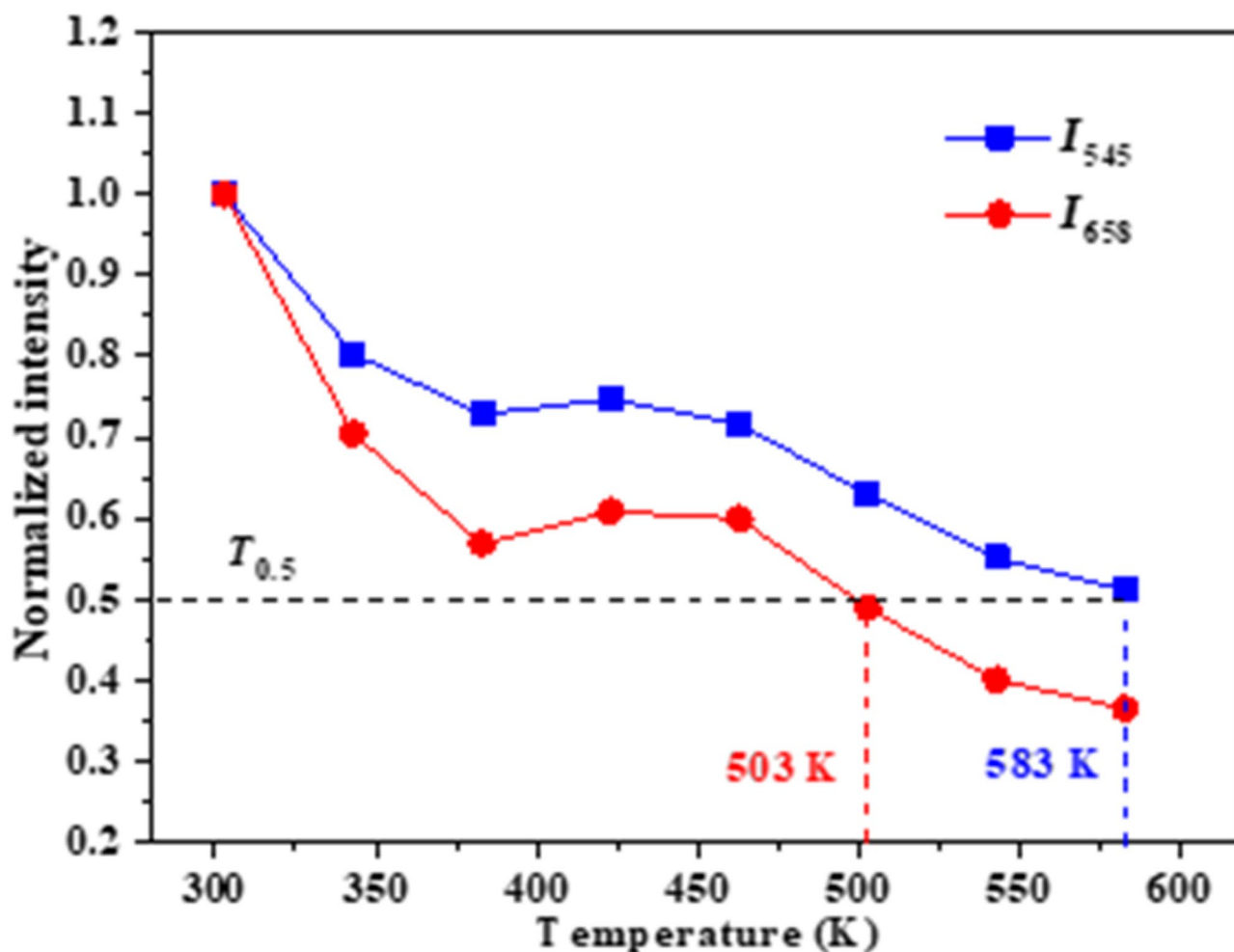


Fig. 10. Normalized integrated intensities (I_{545} and I_{658}) versus temperature.

the crossover process and Eq. (16), we analyzed the relationship between emission intensity and temperature, enabling the calculation of the sample's thermal activation energy²¹.

$$I(T) = \frac{I_0}{1 + A \exp\left(-\frac{\Delta E}{kT}\right)} \quad (15)$$

In this equation, $I(T)$ and I_0 represent the fluorescence intensities at temperature T and the initial fluorescence intensity, respectively; A is a constant; k denotes the Boltzmann constant; and ΔE represents the activation energy. Non-linear fitting of the integrated emission intensities I_{545} and I_{658} at various temperatures yielded results as shown in Fig. 11. The fitting R^2 values were 0.9194 and 0.9109, respectively, indicating that the data fits well with Eq. (16). The fitting results revealed that the thermal activation energies for the green and red transitions are $\Delta E_{545} = 0.4863$ eV and $\Delta E_{658} = 0.4203$ eV, respectively. As the temperature increases, the vibrations between the lattices gradually intensify, which inevitably leads to thermal excitation processes from lower energy levels to higher ones. This results in an increase in the population of the green light energy level $^4S_{3/2}$, with a greater thermal activation energy. The higher activation energy values indicate that the $\text{MgAl}_2\text{O}_4:\text{Er}^{3+}, \text{Yb}^{3+}$ phosphors possess good photothermal stability, with the green light level displaying a higher thermal activation energy than the red, further corroborating the superior photothermal stability of the green emission²².

Conclusion

A series of nanorod $\text{MgAl}_2\text{O}_4:x\text{Er}^{3+}, 0.05\text{Yb}^{3+}$ phosphors were synthesized using a low-temperature hydrothermal method, with the maximum Er^{3+} doping concentration identified at $x=0.015$. As the concentration of Er^{3+} increased, the lattice experienced changes due to the combined effects of vacancy defects and lattice expansion, initially increasing and then decreasing. A calcination temperature of 1100 °C was deemed economically viable, resulting in a total weight loss of 38.5% during the precursor calcination process. Under 980 nm excitation, these phosphors exhibited strong green emissions at 524 nm and 545 nm and a red emission at 658 nm. The intensity and ratio of the red to green emissions peaked at an Er^{3+} doping concentration of 0.01, likely due to potential cross-relaxation processes involving Er^{3+} ions. By adjusting the doping level of Er^{3+} and the pump current of the

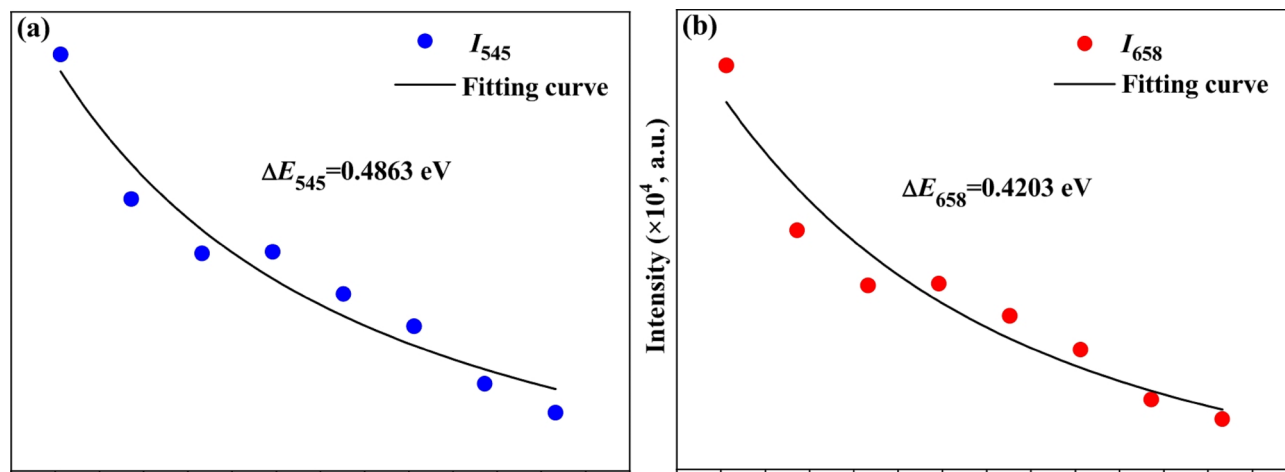


Fig. 11. Nonlinear fitting curves of thermal activation energy for (a) green and (b) red emissions.

excitation light, fine control over the chromatic transition from yellow to green was achieved. The $S_{a_{\max}}$ based on TCLs for Er^{3+} in MgAl_2O_4 was $40.28 \times 10^{-4} \text{ K}^{-1}$, and based on NTCLs, $S_{a_{\max}} = 143.65 \times 10^{-4} \text{ K}^{-1}$, demonstrating superior performance compared to some common upconversion materials. The calculated thermal activation energies for the green and red transitions were $\Delta E_{545} = 0.4863 \text{ eV}$ and $\Delta E_{658} = 0.4203 \text{ eV}$ respectively. The high temperature sensitivity and thermal activation energies indicate that these phosphors are promising candidates for non-contact temperature sensing applications. In addition, with a view to obtaining improved upconversion efficiency and lower toxicity, further exploration of new sensitizers and activators, as well as their practical application in the fields of optical display and temperature measurement, will be necessary.

Data availability

All data generated or analysed during this study are included in this published article.

Received: 9 October 2024; Accepted: 20 March 2025

Published online: 28 March 2025

References

1. Watras, A. et al. Upconversion luminescence properties of nanocrystallite MgAl_2O_4 spinel doped with Ho^{3+} and Yb^{3+} ions. *Opt. Mater.* **34** (12), 2041–2044 (2012).
2. Choudhary, A. K. et al. Enhanced upconversion emission and temperature sensor sensitivity in presence of Bi^{3+} ions in $\text{Er}^{3+}/\text{Yb}^{3+}$ co-doped MgAl_2O_4 phosphor. *Ceram. Int.* **44** (8), 9633–9642 (2018).
3. Sun, L. D., Wang, Y. F. & Yan, C. H. Paradigms and challenges for bioapplication of rare Earth upconversion luminescent nanoparticles: small size and tunable emission/excitation spectra. *Acc. Chem. Res.* **47** (4), 1001–1009 (2014).
4. Gai, S. et al. Recent progress in rare Earth micro/nanocrystals: soft chemical synthesis, luminescent properties, and biomedical applications. *Chem. Rev.* **114** (4), 2343–2389 (2014).
5. Lu, Y. et al. Preparation and upconversion luminescence properties of MgAl_2O_4 : Er^{3+} , Yb^{3+} phosphors. *Chin. J. Inorg. Chem.* **36** (04), 688–694 (2020).
6. Lu, Y. et al. Site occupation and fluorescence properties of MgAl_2O_4 : Eu^{3+} phosphors. *Mater. Sci. Semicond. Process.* **137**, 106233 (2022).
7. Zawrah, M. F., Hamaad, H. & Meky, S. Synthesis and characterization of nano MgAl_2O_4 spinel by the co-precipitated method. *Ceram. Int.* **33** (6), 969–978 (2007).
8. Baruah, B., Bhattacharyya, S. & Sarkar, R. Synthesis of magnesium aluminate spinel-An overview. *Int. J. Appl. Ceram. Technol.* **20** (3), 1331–1349 (2023).
9. Gao, X. L. et al. Room-temperature ultrafast synthesis, morphology and upconversion luminescence of $\text{K}_{0.3}\text{Bi}_{0.7}\text{F}_{2.4}$: $\text{Yb}^{3+}/\text{Er}^{3+}$ nanoparticles for temperature-sensing application. *CrystEngComm* **22** (42), 7066–7074 (2020).
10. Runowski, M. et al. Sr_2LuF_6 : Yb^{3+} - Ho^{3+} - Er^{3+} upconverting nanoparticles as luminescent thermometers in the first, second, and third biological windows. *ACS Appl. Nano Mater.* **3** (7), 6406–6415 (2020).
11. Mahata, M. K. et al. YVO_4 : $\text{Er}^{3+}/\text{Yb}^{3+}$ phosphor as multifunctional applications. *J. Opt. Soc. Am. B: Opt. Phys.* **31** (8), 1814–1821 (2014).
12. Tiwari, S. P. et al. Enhanced temperature sensing response of upconversion luminescence in ZnO-CaTiO_3 : $\text{Er}^{3+}/\text{Yb}^{3+}$ nanocomposite phosphor. *Spectrochim Acta Part. A.* **150**, 623–630 (2015).
13. Goderski, S. et al. Lanthanide upconverted luminescence for simultaneous contactless optical thermometry and manometry sensing under extreme conditions of pressure and temperature. *ACS Appl. Mater. Interfaces.* **12** (36), 40475–40485 (2020).
14. Huang, B. H. et al. Effects of Er^{3+} concentration on upconversion luminescence and temperature sensing properties in $\text{Bi}_4\text{Ge}_3\text{O}_{12}$ crystal. *J. Alloys Compd.* **853**, 156970 (2021).
15. Qiang, Q. & Wang, Y. Enhanced optical temperature sensing and upconversion emissions based on the Mn^{2+} codoped NaGdF_4 : Yb^{3+} , Ho^{3+} nanophosphor. *New J. Chem.* **43** (13), 5011–5019 (2019).
16. Zhang, J., Li, X. & Chen, G. Upconversion luminescence of $\text{Ba}_9\text{Y}_2\text{Si}_6\text{O}_{24}$: Yb^{3+} - Ln^{3+} ($\text{Ln} = \text{Er}, \text{Ho}, \text{ and Tm}$) phosphors for temperature sensing. *Mater. Chem. Phys.* **206**, 40–47 (2018).
17. Zhang, J. & Chen, J. Electronic structure, upconversion luminescence and optical temperature sensing behavior of Yb^{3+} - $\text{Er}^{3+}/\text{Ho}^{3+}$ doped NaLaMgWO_6 . *J. Alloys Compd.* **783**, 84–94 (2019).

18. Lu, H. et al. Optical temperature sensing in β -NaLuF₄: Yb³⁺/Er³⁺/Tm³⁺ based on thermal, quasi-thermal and non-thermal coupling levels. *RSC Adv.* **6** (60), 55307–55311 (2016).
19. Lisiecki, R. & Ryba-Romanowski, W. Silica-based oxyfluoride glass and glass-ceramic doped with Tm³⁺ and Yb³⁺-VUV-VIS-NIR spectroscopy and optical thermometry. *J. Alloys Compd.* **814**, 152304 (2020).
20. He, D. et al. Synthesis and thermometric properties of shuttle-like Er³⁺/Yb³⁺ co-doped NaLa(MoO₄)₂ microstructures. *CrystEngComm* **17** (40), 7745–7753 (2015).
21. Wang, Y. et al. Temperature dependence of red-emitting KLa(MoO₄)₂: Sm³⁺ phosphor. *Chin. J. Lumin.* **35** (4), 1416–1421 (2014).
22. Zhou, J. C. et al. Synthesis and luminescence properties of broadband emitting yellow phosphor Sr₈MgAl(PO₄)₇: xEu²⁺ for white light-emitting diode. *Chin. J. Inorg. Chem.* **37** (7), 1237–1244 (2021).

Acknowledgements

This work was supported by the Liaoning Provincial Natural Science Foundation Yingkou Joint Program (2024LNYKJ05) and the Foundation of Liaoning Provincial Engineering Research Center for High Value Utilization of Magnesite (LMNKY202302, LMNKY202304).

Author contributions

Y.L. is involved in conceptualization, methodology, validation, characterization, formal analysis, investigation, writing-original draft, funding acquisition, visualization. J.W. and G.W. are involved in writing-review & editing, conceptualization, methodology, project administration. Z.S. is involved in conceptualization, methodology, characterization, data curation, writing-review and editing. Y.J. is involved in methodology, formal analysis. C.D. is involved in investigation, writing-editing. All authors read and approved the final manuscript.

Declarations

Competing interests

The authors declare no competing interests.

Additional information

Correspondence and requests for materials should be addressed to J.W. or G.W.

Reprints and permissions information is available at www.nature.com/reprints.

Publisher's note Springer Nature remains neutral with regard to jurisdictional claims in published maps and institutional affiliations.

Open Access This article is licensed under a Creative Commons Attribution-NonCommercial-NoDerivatives 4.0 International License, which permits any non-commercial use, sharing, distribution and reproduction in any medium or format, as long as you give appropriate credit to the original author(s) and the source, provide a link to the Creative Commons licence, and indicate if you modified the licensed material. You do not have permission under this licence to share adapted material derived from this article or parts of it. The images or other third party material in this article are included in the article's Creative Commons licence, unless indicated otherwise in a credit line to the material. If material is not included in the article's Creative Commons licence and your intended use is not permitted by statutory regulation or exceeds the permitted use, you will need to obtain permission directly from the copyright holder. To view a copy of this licence, visit <http://creativecommons.org/licenses/by-nc-nd/4.0/>.

© The Author(s) 2025